atmosphere

MDPI

Article

Integrated Multi-Source Observational Analysis of Successive Light Hail and Moderate Rain Showers at Guiyang Longdongbao International Airport

Guanhan Huang [1], Lian Duan [1], Yaohui Li [1,*], Feng Tang [2], Kaikai Liu [1], Jie Zhang [1], Hao Wan [3] and Qianpeng Wu [4]

[1] China Meteorological Administration Key Laboratory for Aviation Meteorology, Civil Aviation Flight University of China, Chengdu 618307, China
[2] Guizhou Sub-Bureau, Southwest Regional Air Traffic Management Bureau, Civil Aviation Administration of China, Guiyang 550000, China
[3] Beijing Airda Electronic Equipment Co., Ltd., Beijing 100036, China
[4] Sichuan Xiwu Laser Technology Co., Ltd., Chengdu 610041, China
* Correspondence: li-yaohui@163.com; Tel.: +86-139-9318-5923

Abstract

This study compares the environmental conditions and hydrometeor characteristics of successive light hail and moderate rain showers produced by two independent convective cells at Guiyang Airport on 11 April 2025. Automatic weather observations, microwave-radiometer retrievals, wind-profiler measurements, C-band dual-polarization radar data, and ERA5 reanalysis were examined. Before the light hail, the positive-buoyancy layer extended through the 0 to −20 °C hail-growth zone, the equilibrium level was above the −20 °C level, and deep-layer shear and storm-relative helicity were stronger. Its intense echo core extended from 2.5 to 5.0 km, and polarimetric and surface observations indicated mixed rain and hail. Before the moderate rain shower, positive buoyancy was shallower, the equilibrium level was below the −20 °C level, and deep-layer dynamical support was weaker. Its intense echo core was concentrated at 1.6–2.5 km, with signatures dominated by liquid raindrops. For this case, precipitation type differed with the vertical alignment of the buoyancy and hail-growth layers and with the persistence of deep-layer dynamical support. Additional cases are needed to test this interpretation.

Keywords: light hail; moderate rain shower; dual-polarization radar; microwave radiometer; low-level jet

Check for updates

Academic Editors: Sounak Biswas and Eiichi Yoshikawa

Received: 10 August 2026
Revised: 24 September 2026
Accepted: 29 September 2026
Published: 15 October 2026

Copyright: © 2026 by the authors. Licensee MDPI, Basel, Switzerland. This article is an open access article distributed under the terms and conditions of the Creative Commons Attribution (CC BY) license.

1. Introduction

Convective precipitation in airport terminal areas poses a persistent threat to aviation safety and operational continuity. Hazardous hydrometeors, turbulence, abrupt wind shifts, and rapid visibility reductions often occur on scales that conventional forecasts cannot resolve adequately. Hail is particularly hazardous. Even small hailstones can damage windshields, radomes, wing leading edges, and engine components at aircraft operating speeds. Their parent convective clouds may also contain severe turbulence and strong vertical motions [1–3]. Operational risk is not confined to extreme severe convection. Light hail is often embedded in precipitation echoes and can be difficult to distinguish from heavy rain using conventional reflectivity products. A rapid change from light hail to moderate rain showers can also alter runway conditions and arrival or departure decisions within

minutes. Multi-source monitoring and process-based analysis of these events therefore have direct operational value in aviation meteorology.

Several ground-based remote-sensing systems have been used to identify severe convection and monitor its environment. Dual-polarization radar uses reflectivity factor (Z), differential reflectivity (ZDR), copolar correlation coefficient (CC), and specific differential phase (KDP) to characterize particle shape and phase [4–8]. Ground-based microwave radiometers continuously retrieve temperature, water-vapor, and cloud-liquid-water profiles, supporting minute-scale monitoring of instability and convective initiation [9–16]. Wind profiler radars continuously observe lower- and middle-tropospheric winds and low-level jets [17–20]. Their wind-vector profiles also support calculations of vertical wind shear and storm-relative helicity (SRH) [21–24].

Each observing system nevertheless has limitations. Radar reflectivity alone cannot reliably distinguish large raindrops from hail, and C-band Z and ZDR may be attenuated in heavy precipitation [25,26]. Microwave radiometers provide continuous thermodynamic profiles, but precipitation and water on the radome can affect humidity retrievals. Retrieval uncertainty during rainfall therefore requires specific assessment [27]. Wind profiler radar resolves the vertical evolution of winds, but derived jets, shear, and helicity depend on valid sampling heights, data quality, and calculation definitions [28,29]. Radar extrapolation and automated multi-source nowcasting systems have shown the value of combining complementary observations [30–32]. Recent multi-platform and machine-learning studies further demonstrate the complementary value of radar, satellite, surface, and profiler data [33,34]. However, these methods often require large samples, and many studies have focused on extreme hail or widespread heavy rainfall [35]. Continuous observations of local transitions between light hail and rain showers in airport environments remain limited.

For successive airport convective events, the unresolved issue is how thermodynamic instability, vertical wind structure, and hydrometeor characteristics evolve together, particularly how the positive-buoyancy layer is positioned relative to the 0 to −20 °C hail-growth zone and whether deep-layer dynamical support persists. This process-level linkage remains poorly documented for light hail and rain showers produced by separate cells under a common synoptic background. Guiyang Airport lies in complex karst terrain on the eastern flank of the Yunnan–Guizhou Plateau. The plateau's quasi-stationary front and locally terrain-modified airflow frequently produce low cloud, poor visibility, and wind shear. Convective-weather forecasting is difficult, and conventional observations lack the spatial and temporal resolution required for detailed operations. Hail warning consequently remains a persistent challenge for airport weather services.

This study examines successive light-hail and moderate-rain-shower events at Guiyang Airport on 11 April 2025. Microwave-radiometer, wind-profiler, and dual-polarization-radar observations were used to compare two independent convective cells before and during their passage over the same airport within approximately three hours, reducing differences in site and broad synoptic setting. We focus on the configuration of the positive-buoyancy layer relative to the hail-growth temperature zone and on changes in deep-layer shear and SRH. The scientific contribution is the joint linkage of minute-scale thermodynamic profiles, wind diagnostics, and three-dimensional polarimetric structure to the observed hydrometeor types. Cross-checking the independent observations supports a case-specific process interpretation rather than a directly transferable operational threshold.

2. Data and Methods

2.1. Study Area

Because local terrain and instrument placement matter for interpreting the observations, Figure 1a maps the airport's location and surrounding terrain on the eastern Yunnan–Guizhou Plateau, and Figure 1b identifies the principal ground-based observing systems.

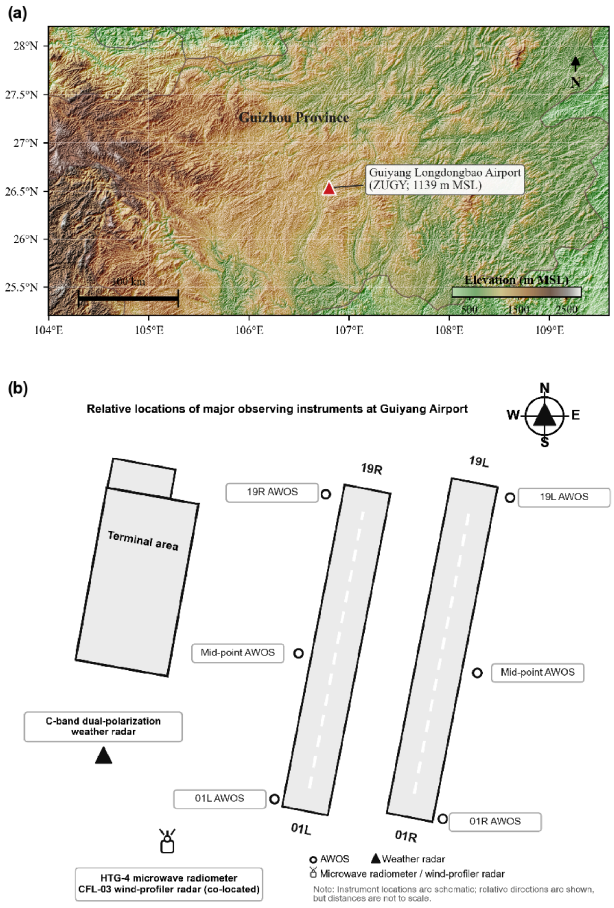


Figure 1. Geographic location, surrounding terrain, and observing instruments at Guiyang Longdongbao Airport. (**a**) Airport location within China and Guizhou Province and the surrounding terrain. Elevations are metres above mean sea level (m MSL). The red area in the inset denotes Guizhou Province, and the red triangle marks the airport. (**b**) Distribution of the main ground-based observing instruments at the airport. Terrain in (**a**) is from Mapzen Terrain Tiles (AWS Open Data; https://registry.opendata.aws/terrain-tiles/; accessed on 24 July 2026), which integrates SRTM, GMTED2010, and ETOPO1. As a static digital-elevation product, it has no daily time dimension. Note: AWOS denotes the Automated Weather Observing System.

Guiyang Longdongbao International Airport (hereafter Guiyang Airport) is located in central Guizhou Province on the eastern Yunnan–Guizhou Plateau. The airport reference point is at 26°32′19″ N, 106°48′03″ E, at an elevation of 1139 m. Mountains, hills, and karst landforms dominate the surrounding area, which has pronounced topographic relief (Figure 1a). The Yunnan–Guizhou quasi-stationary front and local terrain-induced circulations produce substantial spatial variability in lower-tropospheric winds and moisture. This variability complicates the monitoring and forecasting of severe convection at the airport. The airport is oriented approximately north–south and has two parallel runways with azimuths near 10°/190°. These are the western runway 01L/19R and the eastern runway 01R/19L. Figure 1b shows the principal ground-based observing instruments.

2.2. Multi-Source Observations

This study examines a sequence comprising two convective events produced by separate cells that affected the airport successively (Section 3.2). We combined automatic weather observations at Guiyang Airport, nearby ground-based remote sensing, and ECMWF ERA5 reanalysis. The analysis covers near-surface weather, synoptic circulation, thermodynamic profiles and instability, vertical wind structure and dynamics, and three-dimensional microphysical characteristics. The observed variables, spatial and temporal resolutions, and uses of each dataset are described below.

Surface observations were obtained from the Automated Weather Observing System (AWOS) at Guiyang Longdongbao International Airport. Variables included wind direction, wind speed, air temperature, relative humidity, pressure (QFE), visibility, and cloud-base height (CH) at sites along both runways. The AWOS wind sensors acquired and updated measurements every 15 s, whereas the archived meteorological dataset had a 1-minute sampling interval.

ERA5 variables included horizontal wind components (u and v), geopotential height, temperature, and relative humidity. The data had a spatial resolution of 0.25° × 0.25° and a temporal resolution of 1 h. Analyses at 00:00 and 12:00 UTC were selected to characterize the synoptic environment at two key times.

The remote-sensing datasets comprised three systems. A C-band Doppler dual-polarization weather radar was located southwest of the airport at 26.53° N, 106.79° E and 1164 m elevation. It had a 150 km range and an approximately 4.6-minute volume-scan interval, with 4 min 35–36 s between scans. These data were used to identify and track the three-dimensional structure and microphysical characteristics of the convective cells. An HTG-4 ground-based multichannel microwave radiometer was deployed west of Runway 01L. It produced temperature and humidity profiles at 93 vertical levels from the surface to 10 km every 3 min. A co-located CFL-03 boundary-layer wind profiler radar supplied horizontal wind, vertical velocity, and signal-to-noise ratio within its valid 0–5 km range every 6 min. Its vertical resolution was 60 m below 1200 m and 120 m above that height. Unless stated otherwise, all times are Coordinated Universal Time (UTC), and all heights are above ground level (AGL).

The datasets were analyzed together while retaining their original sampling intervals. The 1-minute AWOS record defined the start and end of each precipitation stage. Microwave-radiometer, wind-profiler, and dual-polarization-radar data retained their respective 3-minute, 6-minute, and approximately 4.6-minute resolutions, without averaging or resampling. Observations within each stage were compared by temporal proximity within each instrument's update interval and by physical consistency. Radar data tracked the cells that affected the airport (Section 3.2), while ERA5 described the synoptic environment.

2.3. Quality Control of Microwave-Radiometer Data

Observation times, missing data, physical ranges, and the temporal continuity of thermodynamic profiles, integrated water vapor, and liquid water path were checked before analysis. The radiometer's precipitation-status flag (RainFlag) was also examined because rainfall can bias retrievals. RainFlag = 1 indicates detected precipitation, when hydrometeors on the radome may affect thermodynamic profiles and derived indices. RainFlag = 0 only indicates that the instrument did not detect precipitation; it does not exclude retrieval errors amplified by CAPE integration. RainFlag was therefore not used alone to reject data. Profiles with isolated discontinuities or anomalous vertical structures were checked against contemporaneous radiosonde, AWOS, and radar observations and against adjacent retrievals. Times confirmed as anomalous by multiple sources were

excluded from quantitative analysis. Nearby radiometer retrievals that could be compared with radiosondes provided the main reference for assessing the representative magnitude of CAPE. Data passing these checks were used to analyze thermodynamic structure and convective indices.

2.4. Calculation of Diagnostic Variables

2.4.1. Vertical Wind Shear

Vertical wind shear represents the mean change in the horizontal wind vector across a specified layer. Mean shear magnitudes were calculated for the 0–2 and 0–5 km layers as $S = \Delta V / \Delta z$. Thus, the magnitude of the vector difference between the upper- and lower-boundary winds was divided by the layer depth:

$$S = \frac{|V_2 - V_1|}{(z_2 - z_1)} \quad (1)$$

where V_1 and V_2 are the horizontal wind vectors at heights z_1 and z_2, respectively, where $z_2 > z_1$. Height z is expressed in kilometres, and S therefore has units of m s^{-1} km^{-1}. To account for wind direction, $\Delta V = |V_2 - V_1|$ was calculated using the law of cosines:

$$\Delta V = \sqrt{{V_1}^2 + {V_2}^2 - 2V_1V_2 \cos \alpha} \quad (2)$$

where V_1 and V_2 are the horizontal wind speeds at z_1 and z_2, respectively, in m s^{-1}, and α is the angle between the wind directions in degrees.

2.4.2. Low-Level Jet Index

To represent both LLJ strength below 2 km and its extension toward the surface, we used the empirical index proposed by Liu et al. [36] and adopted by Huang et al. [37]. Both studies defined the lower boundary of the strong-wind layer as the lowest height where wind speed reached 12 m s^{-1}. We retained this criterion because it identified a coherent strong-wind layer in the observed profiles and allowed direct comparison with these regional applications. It is used here as a diagnostic convention, not as a universal LLJ or precipitation-type threshold. The index expresses LLJ strength and downward extension as $I = V/D$:

$$I = \frac{V}{D} \quad (3)$$

where V is the maximum jet-core wind speed below 2 km in m s^{-1}, and D is the lowest height where wind speed reaches 12 m s^{-1} in kilometres. The units of I are m s^{-1} km^{-1}, numerically equivalent to 10^{-3} s^{-1}. D was taken as the lowest qualifying height at or above the radar's lowest valid sampling level. Because this sampling level was above zero, $D > 0$ and the index could not diverge through division by zero. When no wind speed below 2 km reached 12 m s^{-1}, I was recorded as missing. Accordingly, peaks in this index reflect both jet strengthening and downward extension of the strong-wind layer. They are also amplified mathematically because D is the denominator and cannot be interpreted simply as simultaneous wind-speed surges.

2.4.3. Storm-Relative Helicity

Storm-relative helicity (SRH) represents streamwise vorticity in storm-relative flow that can enter an updraft. We applied the discrete hodograph formulation of Davies-Jones [22] after interpolating quality-controlled wind profiles to a 100 m vertical grid. SRH was calculated separately for the 0–2 and 2–5 km AGL layers.

$$\mathrm{SRH} = \sum_{n=0}^{N-1} \left[(u_{n+1} - C_x)(v_n - C_y) - (u_n - C_x)(v_{n+1} - C_y) \right] \quad (4)$$

where N is the number of adjacent wind-layer intervals; u_n and v_n are the zonal and meridional wind components at level n; and $C = (C_x, C_y)$ is the estimated storm-motion vector. Following Shi et al. [38] and Ni et al. [39], C was estimated separately for each integration layer. The height-weighted mean wind vector was rotated 40° to the right while retaining its speed. Because SRH is sensitive to the assumed storm motion, only temporal changes within the same layer were compared.

3. Results

3.1. Applicability of Microwave-Radiometer Retrievals

The radiometer retrievals were evaluated against radiosonde observations at 00:00 and 12:00 UTC. Temperature comparisons are presented in Figure 2a,c, and dew-point comparisons in Figure 2b,d.

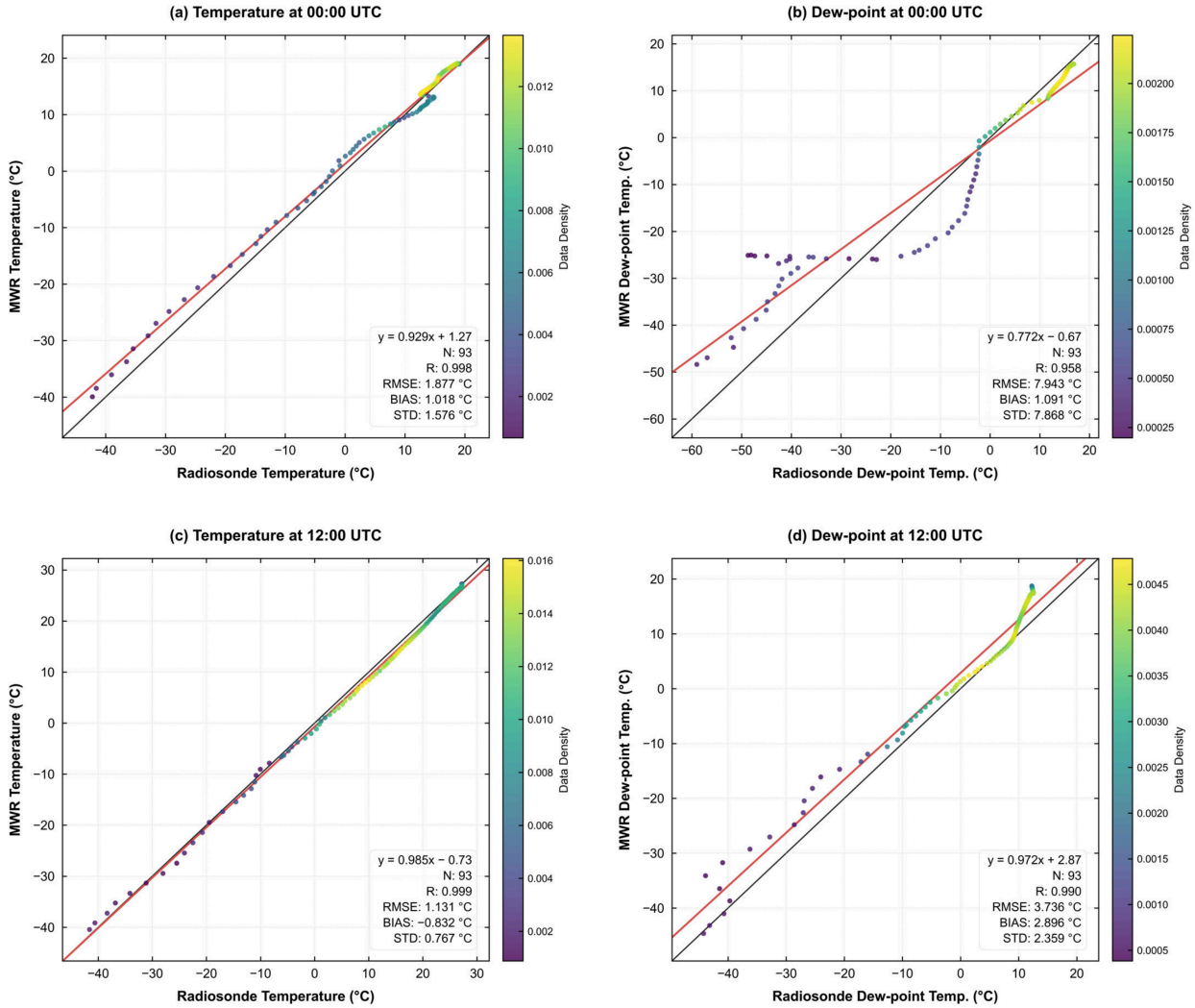


Figure 2. Scatter-density comparisons of atmospheric temperature and dew-point temperature retrieved by the microwave radiometer (MWR) and measured by radiosonde (RS) at 00:00 and 12:00 UTC. The black line is the 1:1 reference, and the red line is the linear regression. Each panel lists sample size (N), correlation coefficient (R), root-mean-square error (RMSE), bias (BIAS), and standard deviation (STD).

Contemporaneous radiosonde observations at 00:00 and 12:00 UTC were used to assess the microwave-radiometer temperature retrievals (Figure 2a,c). Retrieved temperatures clustered closely around the 1:1 line. At 00:00 UTC, R was 0.998, RMSE was 1.877 °C, and the mean warm bias was 1.018 °C. At 12:00 UTC, R was 0.999, RMSE was 1.131 °C, and the mean cold bias was −0.832 °C. These comparisons show that the radiometer reproduced the vertical variation of temperature above the airport well at both times.

The continuous thermodynamic profiles were physically representative and resolved minute-scale changes in temperature and moisture. Dew-point retrievals were more dispersed than temperature retrievals but still captured the overall moisture-profile variation (Figure 2b,d). At 12:00 UTC, R was 0.990, RMSE was 3.736 °C, and the mean moist bias was 2.896 °C. At 00:00 UTC, RMSE and the error standard deviation were 7.943 and 7.868 °C, respectively. CAPE, KI, LI, and SI are sensitive to lower-tropospheric thermodynamic profiles; so, dew-point errors may be amplified in index calculations. As a magnitude check, CAPE from the 12:00 UTC radiosonde and the corresponding radiometer profile was 343.6 and 311.4 J kg^{-1}, respectively, indicating comparable magnitudes.

3.2. Observed Weather and Synoptic Environment

Figure 3 summarizes the precipitation timing and associated near-surface thermodynamic and wind evolution during the two stages.

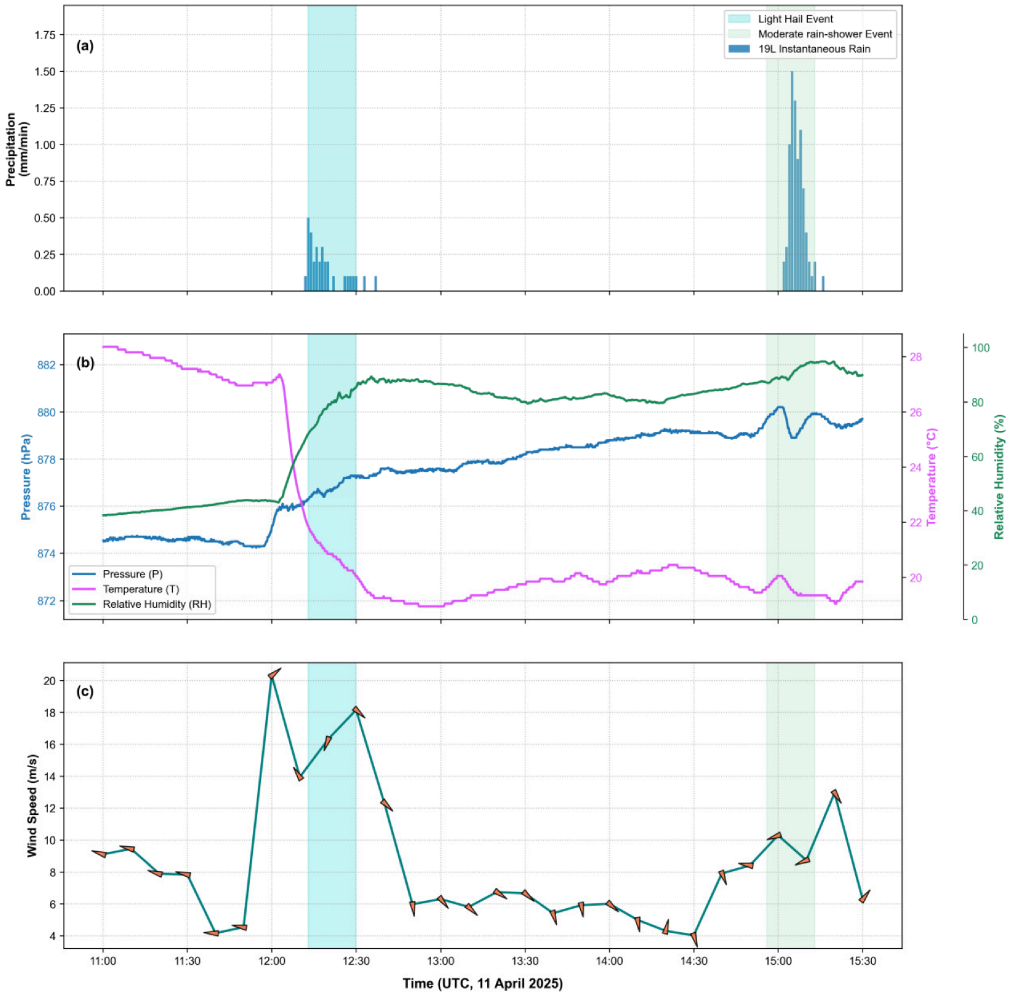


Figure 3. Time series of (**a**) precipitation; (**b**) surface temperature, pressure, and relative humidity; and (**c**) surface wind at Guiyang Longdongbao Airport from 11:00 to 15:30 UTC on 11 April 2025. Blue and green shading denotes the light-hail and moderate-rain-shower periods, respectively.

The precipitation record (Figure 3a) shows that convective clouds affected Guiyang Airport from 11:30 to 15:30 UTC on 11 April 2025, causing seven flight diversions and one return flight. Human observers reported light hail with diameters below 20 mm from 12:13 to 12:30 UTC. Dual-polarization radar simultaneously detected reflectivity above 60 dBZ and mixed rain–hail signatures, consistent with coexisting ice- and liquid-phase hydrometeors. From 14:56 to 15:13 UTC, the AWOS recorded a moderate rain shower with 11.2 mm of rainfall. The analysis focuses on environmental conditions and multi-source observations from 12:13 to 15:13 UTC.

During the first stage, surface pressure increased sharply at 11:58 UTC, and temperature fell by 8.40 °C between 12:04 and 13:00 UTC while relative humidity exceeded 80% at 12:21 UTC (Figure 3b). Surface winds shifted abruptly from easterly to southwesterly and reached 20.3 m s^{-1} (Figure 3c). The pressure rise preceded the cooling by approximately 10 min, consistent with the surface response before and during arrival of the cold-pool outflow [40].

During the second stage, the moderate rain shower occurred from 14:56 to 15:13 UTC (Figure 3a). Relative humidity rose to 94.80%, and surface temperature recovered to 20.00 °C (Figure 3b). After 14:50 UTC, surface pressure fluctuated (Figure 3b). Wind speed increased again to 12.8 m s^{-1}, and wind direction shifted to easterly (Figure 3c).

Dual-polarization radar tracking showed that the light-hail cell formed over Nayong County at 09:58 UTC. At 12:01 UTC, when its intense echo area entered the airport, the maximum composite reflectivity was 58.5 dBZ. This time- and area-specific value differs from the earlier cell-centered local maximum of 67.5 dBZ observed at 11:24 UTC, when the cell was at azimuths of 295.06–316.55° and ranges of 39–42 km from the radar (Section 3.5). The moderate-rain-shower cell formed south of Nayong County at 11:47 UTC and reached the airport at 14:52 UTC. The two cells had different formation times and tracks and affected the airport successively. Thus, the observed "transition" describes the chronological change in surface weather, not a phase transition within one cell. The following analysis compares the thermodynamic, dynamical, and microphysical environments preceding the two events.

The ERA5 fields compare the circulation at 00:00 UTC (Figure 4a–c) with that at 12:00 UTC (Figure 4d–f), providing the synoptic context for the successive passage of the two cells.

The successive light-hail and moderate-rain-shower events occurred as a Mongolian cyclone and its upper-level trough gradually extended southward. Figure 4 shows the environmental evolution between 00:00 and 12:00 UTC.

At 00:00 UTC, an upper-level frontal zone lay along the southern flank of the Mongolian cyclone at 500 hPa. The upper-level trough extended southward, placing Guiyang in westerly flow ahead of the trough (Figure 4a). At 700 hPa, warm, moist southwesterly flow met dry, cold air north of Guiyang and formed a shear line. The airport was south of this line (Figure 4b). At 850 hPa, persistent southwesterly flow transported moisture, and the airport lay within an area of relative humidity above 80% (Figure 4c). This vertical arrangement of upper-level dry, cold air over lower-level warm, moist air provided favorable moisture and stratification for convection.

By 12:00 UTC, the Mongolian cyclone and upper-level trough had moved markedly eastward and southward. The upper-level frontal zone near the trough base appeared stronger (Figure 4d), and the 700 and 850 hPa shear lines had advanced southward. Closely spaced isotherms intersected the height contours at larger angles near the shear line, qualitatively indicating a stronger horizontal temperature gradient and baroclinic zone. The juxtaposition of dry, cold air and warm, moist southwesterly flow near the airport was also consistent with enhanced low-level moisture confluence and an environment favorable for ascent (Figure 4e,f). Because frontogenesis, moisture-flux convergence, and vertical

motion were not calculated explicitly, these ERA5 patterns are interpreted as qualitative background rather than quantitative attribution.

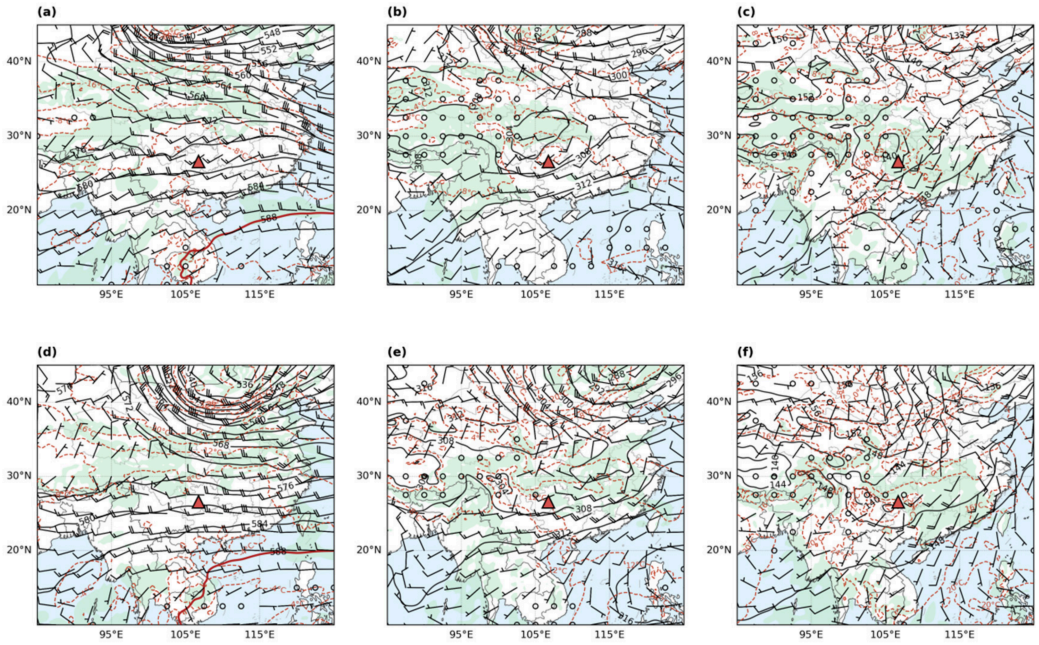


Figure 4. ERA5 geopotential height (black solid contours; dagpm), temperature (red dashed contours; °C), and horizontal winds (wind barbs; m s^{-1}) at 500 hPa (**a**,**d**), 700 hPa (**b**,**e**), and 850 hPa (**c**,**f**) at 00:00 UTC (**a**–**c**) and 12:00 UTC (**d**–**f**) on 11 April 2025. Light-green shading indicates relative humidity above 80%, and the red triangle marks Guiyang Longdongbao Airport.

3.3. Evolution of the Thermodynamic Structure

Microwave-radiometer observations at Guiyang Airport were used to examine the continuous evolution of thermodynamic profiles, liquid water, and instability.

3.3.1. Boundary-Layer and Tropospheric Temperature

The time–height temperature field was examined to compare the vertical thermal evolution of the two stages (Figure 5).

Before and during the light-hail event (11:45–12:20 UTC), the temperature field in Figure 5 shows that temperature at 2 km first decreased from 11.50 to 8.19 °C between 11:45 and 12:02 UTC, then recovered to 10.80 °C. At 8 km, temperature decreased from −25.78 to −29.29 °C before recovering to −26.56 °C. Temperature contours descended markedly during the light hail from 12:13 to 12:30 UTC. Together with surface cooling, the pressure jump, and the abrupt wind shift, this descent indicated a pronounced lower-tropospheric response to subsiding cold air and cold-pool outflow.

Before and during the moderate rain shower (14:45–15:06 UTC), Figure 5 shows that temperature at 2 km decreased from 10.72 to 7.26 °C before rising to 14.53 °C. At 8 km, temperature decreased from −25.61 to −28.55 °C and then recovered to −22.71 °C. The temperature disturbance was shorter-lived, and the isotherms recovered rapidly. Thermodynamic adjustment was therefore faster than during the light-hail stage.

Cooling rates at 2 and 8 km during the light-hail stage were approximately 0.20 and 0.21 °C min^{-1}, respectively. They were lower than the corresponding rates of 0.43 and 0.29 °C min^{-1} during the moderate-rain-shower stage. However, the temperature disturbance persisted longer during light hail, indicating that this convective system affected the airport for a longer period. Temperature changed and recovered more rapidly during the moderate rain shower.

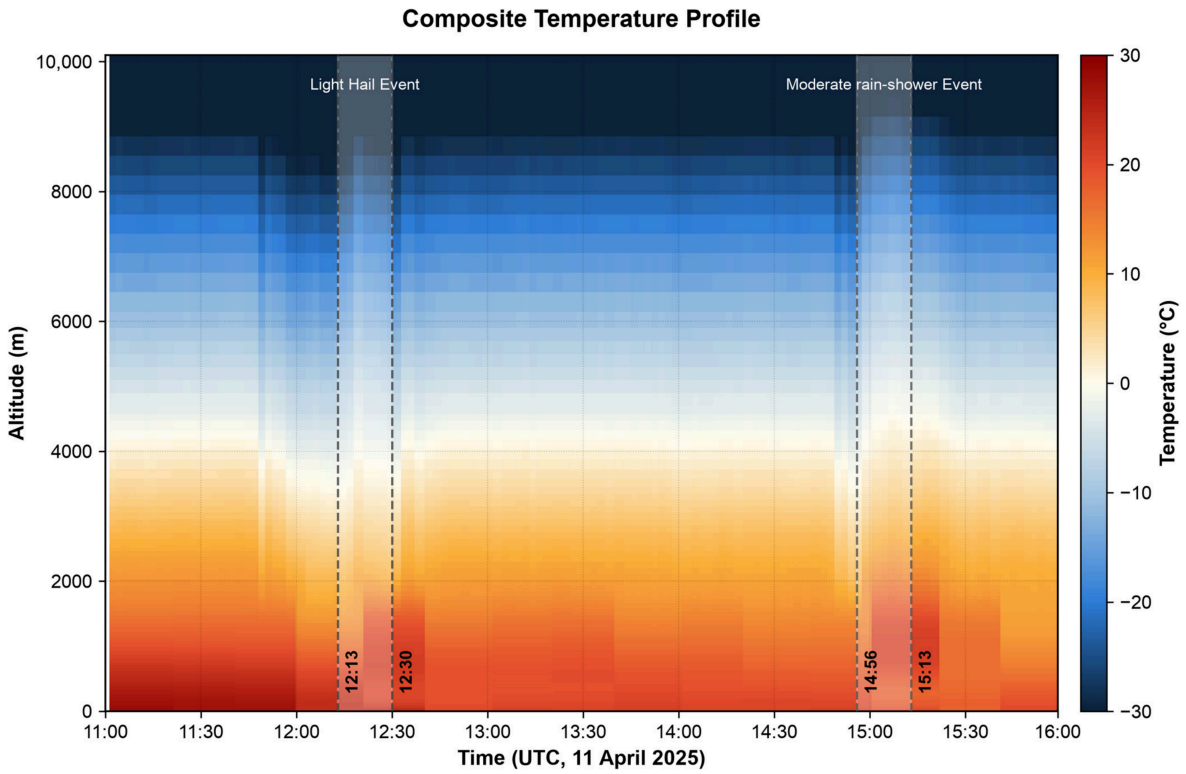


Figure 5. Time–height cross section of composite temperature retrieved by the microwave radiometer at Guiyang Longdongbao Airport from 11:00 to 16:00 UTC on 11 April 2025. Black and gray dashed lines mark the onset and end of the light-hail and moderate-rain-shower periods, respectively.

3.3.2. Liquid Water Distribution

The liquid-water-content field was then used to compare the depth and persistence of condensate before and during the two precipitation stages (Figure 6).

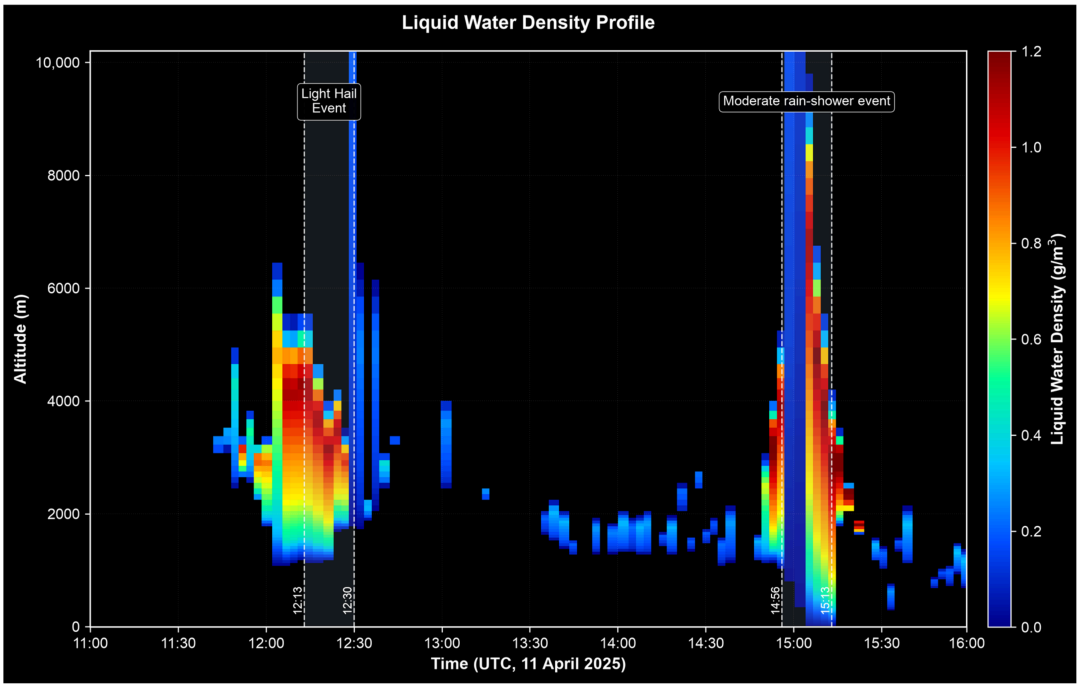


Figure 6. Time–height distribution of liquid water content retrieved by the microwave radiometer at Guiyang Longdongbao Airport from 11:00 to 16:00 UTC on 11 April 2025. Grey dashed lines indicate the light-hail event, and white dash-dotted lines indicate the moderate-rain-shower event.

Figure 6 shows that liquid water content was generally low between 1250 and 6000 m before the event. From 11:41 UTC, a high-value region developed rapidly through this layer, with values reaching 0.8 g m^{-3} between 2000 and 5000 m. This region substantially overlapped the −20 to 0 °C hail-growth zone, indicating rapid cloud deepening into the ice-growth layer. After the light hail ended, the top of the high-value region gradually descended. The liquid-water region expanded again near 14:48 UTC, but its cores were dispersed and short-lived, then weakened rapidly with the precipitation.

During the light-hail stage, enhanced liquid water in Figure 6 persisted longer and was concentrated mainly at 2000–5000 m, with a maximum near 1.16 g m^{-3}. This region overlapped the 0 to −20 °C hail-growth zone. During the moderate-rain-shower stage, enhanced liquid water was shorter-lived and more dispersed, and its overlap with the hail-growth zone was less extensive and persistent.

3.3.3. Thermodynamic Diagrams

The pre-event thermodynamic structures are compared using the 11:57:58 UTC profile before light hail (Figure 7a) and the 14:48:53 UTC profile before the moderate rain shower (Figure 7b).

Before the light hail (Figure 7a), the microwave radiometer retrieved CAPE of 1690.8 J kg^{-1} at 11:57 UTC and a level of free convection (LFC) at 744 hPa. RainFlag was not activated, and no surface precipitation occurred at that time. Thus, there was no evidence that a wet radome affected this value. CAPE from the 12:00 UTC radiosonde and 12:01:49 UTC radiometer retrieval was 343.6 and 311.4 J kg^{-1}, respectively. The large radiometer change between 11:57 and 12:01 UTC reflects substantial minute-scale variability. It may include both rapid local adjustment and retrieval sensitivity to thermodynamic perturbations, which cannot be separated quantitatively using one site. The following analysis therefore emphasizes buoyant-layer depth, moist-layer structure, and their configuration relative to the hail-growth zone. Weak convective inhibition (CIN) extended from the surface to 750 hPa. Hail grows mainly by accretion of supercooled liquid water onto embryos, with most mass growth occurring between 0 and −20 °C [41–43]. At 11:57 UTC, the equilibrium level (EL) was at 242 hPa, or approximately 10,556 m, above the −20 °C level at 364 hPa and 7635 m. The positive-buoyancy layer spanned the 0 to −20 °C hail-growth zone from 567 to 364 hPa, a depth of approximately 3010 m. A near-saturated layer from 613 to 324 hPa also extended through this zone. Its depth below 3.15 km agrees with the relatively thin 0 to −20 °C layer reported for hail environments [44]. The buoyant-layer depth and vertical moisture distribution were therefore favorable for ice-particle growth before the light hail.

Sixteen minutes before the moderate rain shower, CAPE had fallen to nearly 0 J kg^{-1} at 14:40 UTC. The 14:48 UTC profile showed weak instability, with CAPE of 168.9 J kg^{-1} (Figure 7b). The EL was at 498 hPa and approximately 5599 m, only about 974 m above the 0 °C level. It was below the −20 °C level at 353 hPa and 8648 m, limiting overlap between positive buoyancy and the main hail-growth zone. The 0 to −20 °C layer deepened to 4023 m, and its upper boundary was markedly higher than during light hail. These features agree with the thicker and higher layer reported for non-hail precipitation environments [44]. The lifting condensation level was at 853 hPa and approximately 1426 m. The temperature and dew-point profiles were close, indicating abundant lower-tropospheric moisture. However, small CAPE and a low EL were unfavorable for sustained deep convection. This thermodynamic configuration provides a physically plausible explanation for restricted ice-particle growth during the moderate rain shower.

Moisture availability alone did not explain the difference in precipitation type. The light-hail stage had a deep positive-buoyancy layer and a near-saturated layer spanning

the 0 to −20 °C zone. The moderate-rain-shower stage had a shallower and less persistent positive-buoyancy layer. Together with the radar and surface observations, these environmental differences explain plausibly why the first cell produced light hail and the second produced a moderate rain shower.

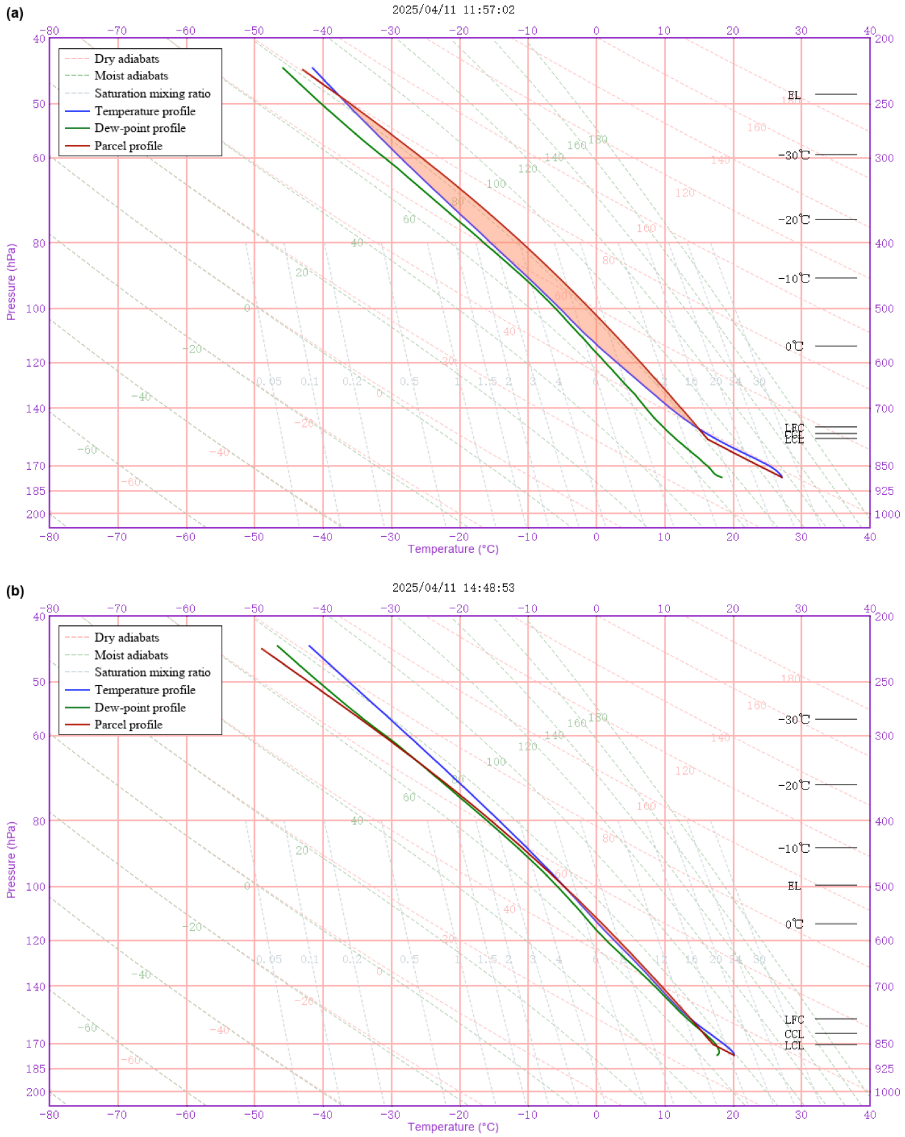


Figure 7. T–ln p diagrams and cloud-layer identification at Guiyang Longdongbao Airport at (**a**) 11:57:58 UTC and (**b**) 14:48:53 UTC. CBH denotes cloud-base height. The left shaded region indicates T − Td ≤ 3 °C, and the right shaded region indicates relative humidity ≥ 80%.

3.3.4. Convective Indices

To characterize the thermodynamic structure resolved by the high-frequency microwave-radiometer profiles, we calculated several instability indices (Figure 8). These were the K index (KI), lifted index (LI), total totals index (TTI), Showalter index (SI), and convective available potential energy (CAPE). Their evolution was compared between the light-hail and moderate-rain-shower stages.

During the light-hail stage (12:13–12:30 UTC), TTI and KI reached 54.94 and 58.2 at 12:15 UTC, respectively. LI and SI fell to −7.9 and −7.4 at 12:14 UTC, respectively. CAPE from the 12:00 UTC radiosonde and nearby 12:01:49 UTC radiometer retrieval was 343.6 and 311.4 J kg^{-1}, respectively. During the moderate-rain-shower stage (14:56–15:13 UTC), TTI peaked at 48.27, while LI and SI reached minima of −5.9 and −5.6. Radiometer-derived

CAPE at 14:48 UTC was 168.9 J kg^{-1}. Minute-scale instantaneous peaks were excluded from quantitative analysis according to the rules in Section 2.3. Between the two stages (12:42–14:48 UTC), CAPE was generally below 250 J kg^{-1}. Instability near the airport therefore remained low after passage of the first cell.

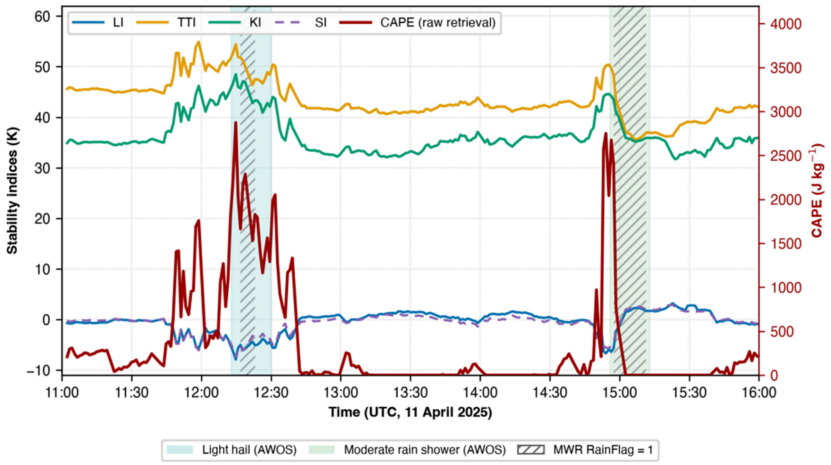


Figure 8. Time series of stability indices (LI, TTI, KI, and SI) and CAPE calculated from MWR-retrieved profiles between 11:00 and 16:00 UTC on 11 April 2025. Blue and green shading denotes the light-hail and moderate-rain-shower periods recorded by the AWOS, respectively. Hatched shading marks periods when the MWR precipitation flag was active (RainFlag = 1).

Among the relatively reliable pre-precipitation observations, CAPE was higher before the light hail than before the moderate rain shower. The vertical profiles in Figure 7 also show deeper positive buoyancy and greater overlap with the 0 to −20 °C hail-growth zone during light hail. Both instability and the depth of convection were more limited before the moderate rain shower. Changes in TTI, KI, LI, SI, and CAPE help describe the thermodynamic environment in this case. However, no single index or isolated peak can determine precipitation phase without thermodynamic profiles, wind structure, and radar observations.

3.4. Evolution of the Dynamical Structure

3.4.1. Horizontal and Vertical Winds

Wind-profiler observations resolve the concurrent evolution of horizontal flow (Figure 9a) and vertical motion (Figure 9b) from 11:00 to 16:00 UTC.

Wind-profiler observations from 0 to 5 km documented the event's dynamical evolution between 11:00 and 16:00 UTC (Figure 9a). Southerly winds predominated below 1 km after 11:00 UTC. From 11:18 UTC, the approximately 12 m s^{-1} isotach extended downward, establishing an LLJ between 500 and 2000 m. During the light hail, the jet core descended as low-level winds strengthened. This pattern is consistent with downward transfer of mid- and lower-tropospheric momentum. Figure 9b shows descent at approximately 0.8–1.1 km and 3.3–5.0 km during light hail. At 12:42 UTC, lower-level descent extended toward the surface as winds shifted to northwesterly. The simultaneous pressure jump and temperature decrease were consistent with passage of a cold-pool outflow boundary [40].

After 12:54 UTC, northerly winds below 1 km coexisted with southerly flow aloft, producing strong directional shear. After 13:30 UTC, the upper extent of descent gradually lowered, the LLJ persisted, and the directional-shear layer rose slightly. During the moderate rain shower, the 0–2 km LLJ core reached approximately 18.9–19.1 m s^{-1}. The directional-shear layer varied between 2800 and 3500 m. From 14:30 UTC, winds above and below a shear layer near 1200 m changed configuration, and the associated descent

was weak. Compared with the light-hail stage, this descent was weaker and spanned a narrower vertical range (Figure 9a,b).

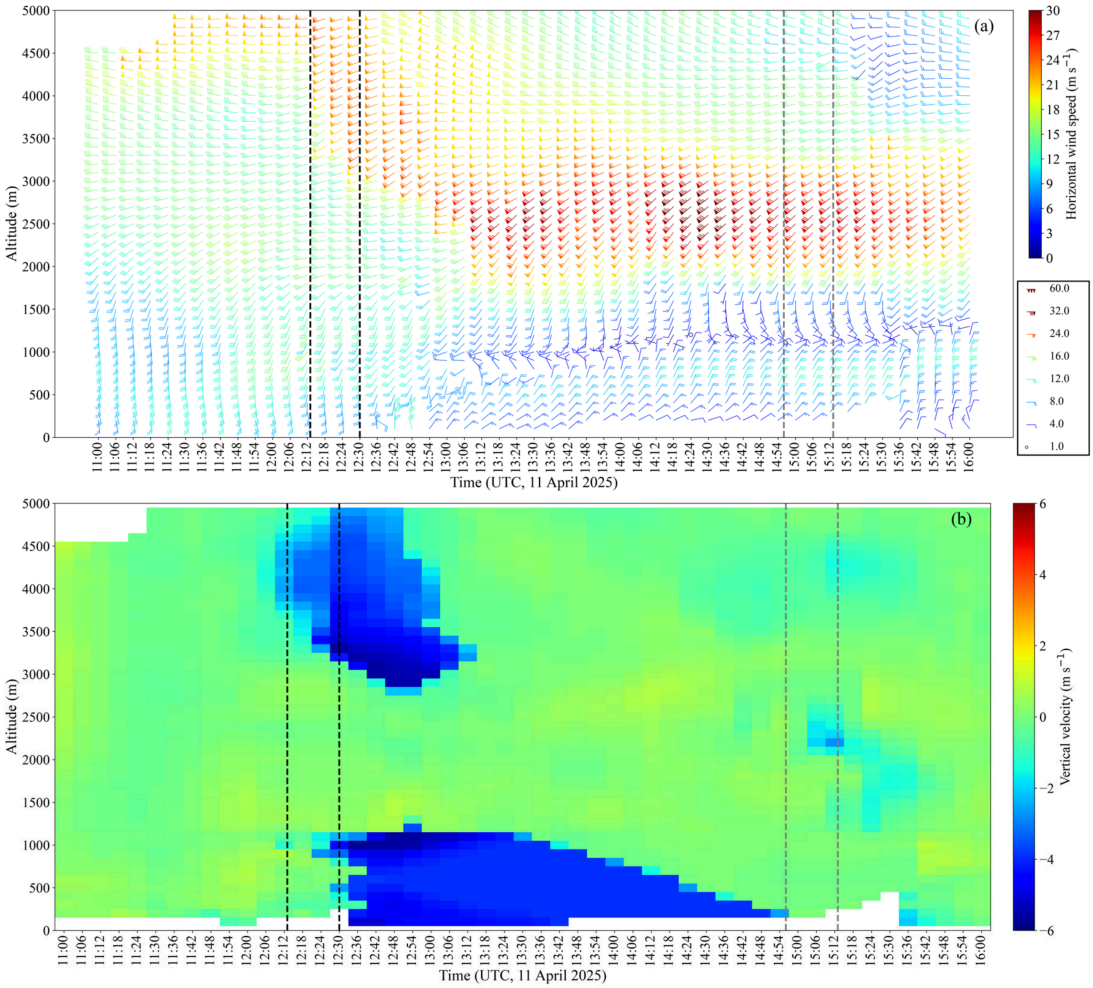


Figure 9. Time–height cross sections of (**a**) horizontal wind and (**b**) vertical velocity observed by the wind profiler radar at Guiyang Longdongbao Airport from 11:00 to 16:00 UTC on 11 April 2025. Black and gray dashed lines mark the onset and end of the light-hail and moderate-rain-shower periods, respectively.

The LLJ persisted throughout the observation period, but jet-core height, directional-shear layers, and descent differed between stages. During light hail, descent occurred at approximately 0.8–1.1 and 3.3–5.0 km, spanning a broad vertical range and accompanying a distinct surface cold-pool response. During the moderate rain shower, negative vertical velocity was concentrated mainly near 2.0–2.5 km, with weaker variations above 3 km.

3.4.2. Dynamical Diagnostic Variables

Guiyang Airport lies at approximately 1139 m elevation on the eastern Yunnan–Guizhou Plateau. All heights used for the dynamical variables are AGL. The 0–2 km layer represents low-level inflow, vertical wind-speed variation, and storm-relative rotation within and above the convective boundary layer. The 0–5 km layer describes the deeper dynamical environment extending from the lower to middle troposphere. SRH was further divided into 0–2 and 2–5 km layers to distinguish lower- and middle-level rotational potential between precipitation stages. Given the airport elevation, 0–2 and 0–5 km AGL correspond approximately to 1.14–3.14 and 1.14–6.14 km MSL, respectively.

The diagnosed dynamical variables are compared across the two stages using vertical wind shear (Figure 10a), LLJI (Figure 10b), and SRH (Figure 10c).

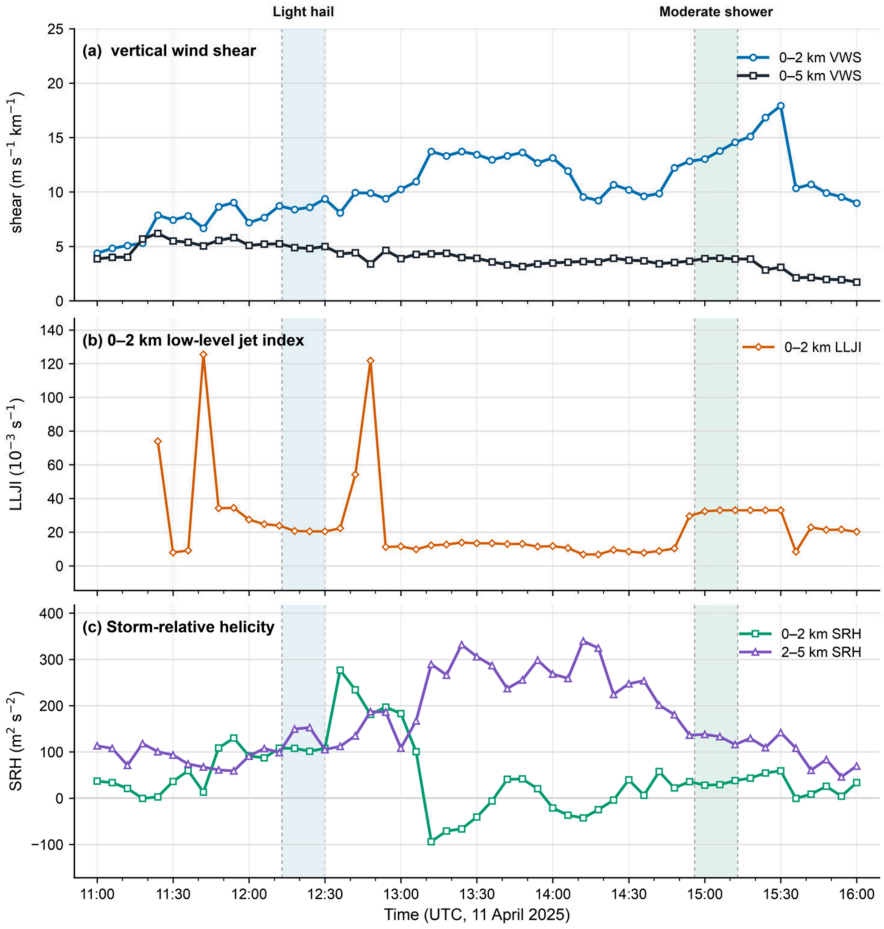


Figure 10. Time series of (**a**) 0–2 and 0–5 km layer-mean vertical wind shear, (**b**) the 0–2 km low-level jet index, and (**c**) 0–2 and 2–5 km storm-relative helicity at Guiyang Longdongbao Airport from 11:00 to 16:00 UTC on 11 April 2025. Blue and green shading denotes the light-hail and moderate-rain-shower periods, respectively. Heights are AGL.

Vertical wind shear differed markedly between the two stages (Figure 10a). During light hail, 0–5 km mean shear remained at 4.8–5.0 m s^{-1} km^{-1}, while 0–2 km shear was 8.4–9.4 m s^{-1} km^{-1}. This configuration favored updraft tilting and maintenance of convective organization. During the moderate rain shower, shear became increasingly confined to lower levels. Shear at 0–2 km increased to 13.0–14.6 m s^{-1} km^{-1}, whereas 0–5 km shear decreased to 3.85–3.92 m s^{-1} km^{-1}. Deep-layer dynamical support for the convective system was therefore weaker.

From 11:00 to 11:18 UTC, maximum wind speed below 2 km did not reach 12 m s^{-1} (Figure 10b). The lower boundary D of the strong-wind layer could not be identified; so, LLJI was missing. LLJI reached 125.5 $\times$ 10^{-3} s^{-1} at 11:42 UTC before light hail and 121.8 $\times$ 10^{-3} s^{-1} at 12:48 UTC after it ended. Both peaks coincided with downward movement of the 12 m s^{-1} wind region, consistent with downward momentum transfer. Because D is the denominator, a strong-wind boundary near the surface also amplifies the index. During the moderate rain shower, LLJI remained at 32.3–32.9 $\times$ 10^{-3} s^{-1}. This range mainly reflected stronger winds below 2 km and descent of the strong-wind region.

Storm-relative helicity also evolved differently between stages (Figure 10c). SRH in both layers generally increased before and during the light hail. After the hail ended, 0–2 km SRH increased briefly, while 2–5 km SRH remained elevated. Before and during

the moderate rain shower, 2–5 km SRH generally decreased, while 0–2 km SRH varied only slightly. Both layers remained below their values during light hail.

The light-hail stage combined deeper vertical shear with persistently higher SRH, supporting greater vertical development of the convective cell. Although low-level shear was strong during the moderate rain shower, deep-layer shear and environmental vorticity support weakened markedly. These conditions were unfavorable for sustained deep convection.

3.5. Dual-Polarization Radar Observations

The plan-position polarimetric structure of the light-hail cell at 11:24 UTC is shown in Figure 11.

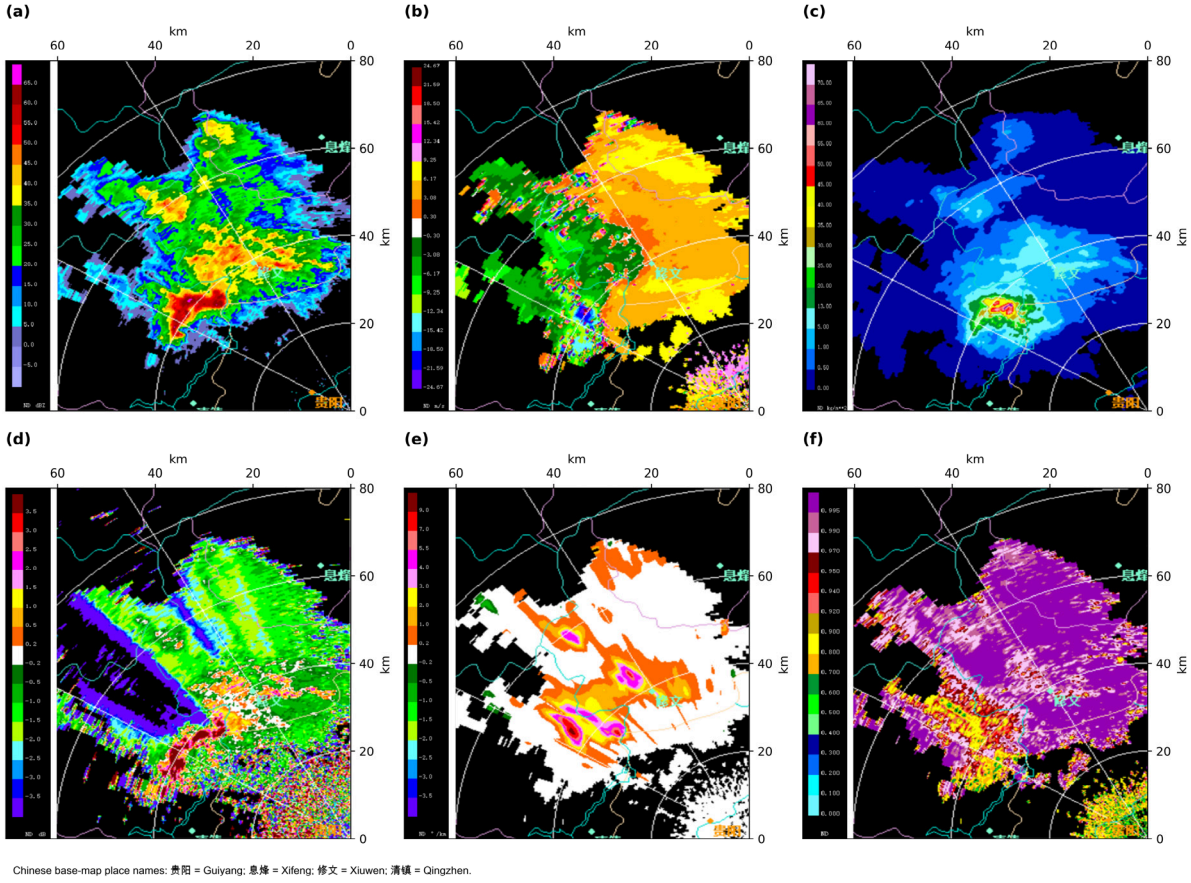


Figure 11. Dual-polarization weather-radar PPI products before the light-hail stage at Guiyang Longdongbao Airport at 11:24 UTC on 11 April 2025. (**a**) Z; (**b**) V; (**c**) VIL; (**d**) Z_{DR}; (**e**) K_{DP}; (**f**) CC.

For comparison, Figure 12 shows the plan-position polarimetric structure of the moderate-rain-shower cell at 14:33 UTC.

The corresponding vertical reflectivity structures of the two cells are compared in Figure 13.

At 11:24 UTC on 11 April 2025, dual-polarization radar detected an intense convective cell at azimuths of 295.06–316.55° and ranges of 39–42 km. The echo was V-shaped, with core reflectivity above 50 dBZ and a local maximum of 67.5 dBZ (Figure 11a). This earlier cell-centered maximum was measured 37 min before the echo entered the airport; the 58.5 dBZ value in Section 3.2 instead refers to the maximum composite reflectivity at 12:01 UTC. The two values therefore describe different times and spatial domains. ZDR ranged from −2.7 to 5.96 dB in a dipolar pattern (Figure 11d). Near-zero and negative values may represent large ice particles or vertically oriented particles, whereas positive

values are mainly consistent with oblate raindrops. CC was generally 0.7–0.9 and fell below 0.68 on the northwestern side (Figure 11f), indicating substantial heterogeneity in particle phase and shape. KDP varied locally from −0.03 to 9.14° km^{-1} (Figure 11e). Positive maxima adjacent to high ZDR indicated contributions from large raindrops. Near-zero and negative values, together with anomalous ZDR and CC, indicated mixed rain and hail. The vertical cross section (Figure 13a) showed that the >60 dBZ core was concentrated at 2.5–5.0 km, overlapping the 0 to −10 °C layer. The surrounding 50 dBZ echo extended to approximately 8.5 km near the −20 °C level. Thus, intense echoes occupied a deep ice-growth layer, consistent with the cell's greater vertical development. Consistent with this stronger and deeper echo structure, the maximum VIL exceeded 60 kg m^{-2} within the light-hail cell (Figure 11c).

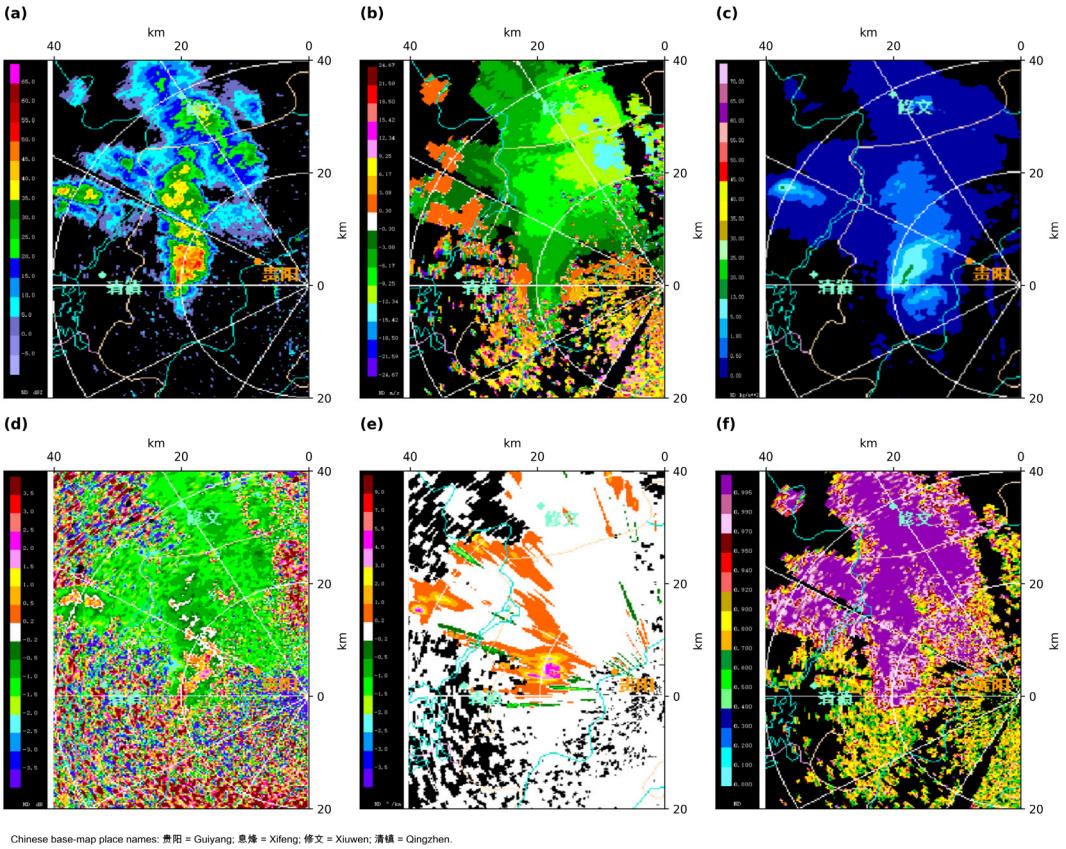


Figure 12. Dual-polarization weather-radar PPI products before the moderate-rain-shower stage at Guiyang Longdongbao Airport at 14:33 UTC on 11 April 2025. (**a**) Z; (**b**) V; (**c**) VIL; (**d**) Z_{DR}; (**e**) K_{DP}; (**f**) CC.

At 14:33 UTC, mesoscale convective echoes occurred at ranges of 15–30 km and azimuths of 253.30–321.04° (Figure 12a). Reflectivity was generally 35–45 dBZ, with a local maximum of 57.5 dBZ (Figure 12a). ZDR was predominantly positive and reached 3.41 dB (Figure 12d), CC was mostly above 0.98 (Figure 12f), and KDP ranged from 0.29 to 5.68° km^{-1} (Figure 12e). This combination is more consistent with predominantly liquid raindrops and a comparatively homogeneous particle phase. The velocity field showed only localized convergence (Figure 12b). The vertical cross section placed the 50 dBZ core mainly at 1.6–2.5 km near the 0 °C level (Figure 13b). Its extension toward the −20 °C ice-growth layer was much weaker than during light hail. The observations were consistent with shallow convection embedded within stratiform echo. By contrast, the maximum VIL of the moderate-rain-shower cell remained below 20 kg m^{-2} (Figure 12c).

The light-hail cell was stronger and developed more deeply. Its ZDR dipole, low-CC region, and local KDP variability were characteristic of mixed-phase precipitation. Echoes during the moderate rain shower were weaker, and their ZDR, CC, and KDP signatures indicated a more homogeneous population of liquid raindrops.

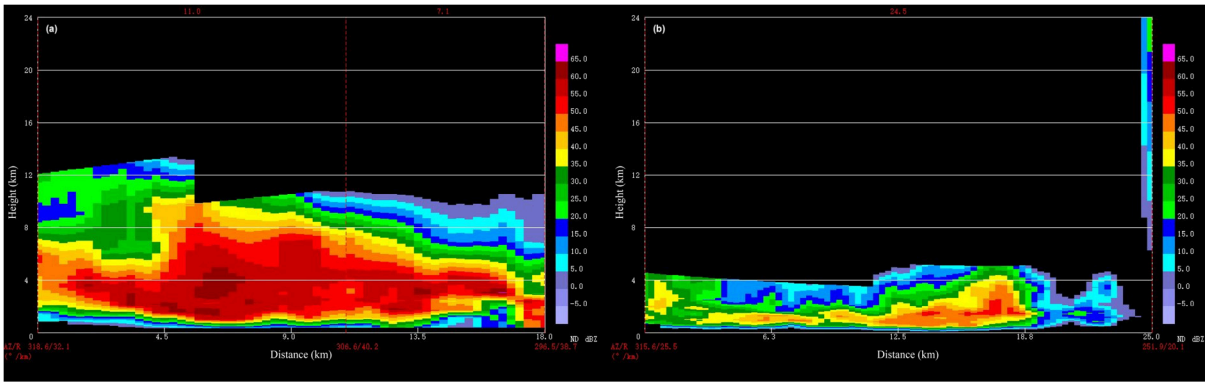


Figure 13. Vertical cross sections of dual-polarization weather-radar reflectivity at Guiyang Longdongbao Airport on 11 April 2025: (**a**) 11:24 UTC before the light-hail stage, corresponding to Figure 11; (**b**) 14:33 UTC before the moderate-rain-shower stage, corresponding to Figure 12.

4. Discussion

Radar-echo tracking showed that two independent convective cells produced the light hail and moderate rain shower as they passed the airport successively. They shared a similar synoptic setting but encountered different local environments before reaching the airport. The combined thermodynamic, dynamical, and radar evidence indicates that their different precipitation types did not depend on one stability index crossing a fixed threshold. Instead, the main differences were the depth of positive buoyancy, its configuration relative to the 0 to −20 °C hail-growth zone, and the persistence of deep-layer shear and SRH. The positive-buoyancy layer in the light-hail cell spanned the hail-growth zone, and the EL was above the −20 °C level. This structure coincided with comparatively deep vertical shear. Before the moderate rain shower, positive buoyancy was shallower, the EL was below the −20 °C level, and deep-layer dynamical support was weaker. This configuration is consistent with statistical findings that hail commonly forms within a deep ice-growth region accompanied by appreciable deep-layer shear [41–44]. However, CAPE from the 12:00 UTC sounding before light hail was only 343.6 J kg^{-1}. In complex terrain, the configuration of buoyancy and the growth zone, together with persistent dynamical support, may therefore be more informative than instantaneous CAPE alone. We hypothesize that reduced thermodynamic buoyancy and weaker deep-layer support limited sustained ice-particle growth, contributing to the observed difference between the two cells. Numerical experiments are needed to separate the contributions of these factors.

The radiosonde comparison supports using the microwave radiometer to examine relative changes in pre-event thermodynamic structure, while also defining the limits of that interpretation. Temperature profiles agreed closely, but the larger dew-point uncertainty can be amplified in derived indices. The comparable radiosonde and radiometer CAPE magnitudes near 12:00 UTC support the broad characterization of instability before the light hail; they do not validate individual minute-scale peaks or an exact precipitation-type threshold. During rainfall, water on the radome can further distort retrieved profiles, and post-passage variability may contain both retrieval effects and genuine environmental adjustment. We therefore give greater weight to temporal continuity, buoyant-layer depth and configuration, and consistency with radiosonde, AWOS, and radar observations than to any single retrieved index value.

Polarimetric variables must be interpreted jointly. During light hail, contrasting positive and negative ZDR, low CC, and local KDP variability agreed qualitatively with reported hail and mixed rain–hail signatures [4–8]. These signatures were also supported by the surface hail report. During the moderate rain shower, positive ZDR, high CC, and comparatively uniform positive KDP indicated liquid raindrops. Neither high reflectivity nor any single polarimetric variable can identify hail independently. Because C-band radar may experience attenuation and differential attenuation in heavy precipitation [25,26], we infer only bulk hydrometeor characteristics from the joint variations.

The low-level jet index $I = V/D$ depends on both jet-core wind speed V and the lower-boundary height D of the strong-wind layer. The two light-hail-stage peaks coincided with descent of the strong-wind layer and therefore had a physical basis. However, a small D mathematically amplifies the index because it is the denominator. The index is used only as a supplementary measure of LLJ evolution and must be interpreted with V, D, and the full wind profile. Its peaks should not be treated as statistically validated operational thresholds.

This study examines one event at an airport in complex terrain. The reported ranges are case-specific and local; so, they cannot establish a general criterion for precipitation phase. Future work should expand the convective-event sample and apply consistent microwave-radiometer quality control and C-band radar attenuation correction. High-resolution numerical simulations are also needed to test the stability and applicability of the proposed configuration and diagnostic variables.

5. Conclusions

ERA5 reanalysis, AWOS, microwave-radiometer, wind-profiler, and C-band dual-polarization-radar data were combined to examine successive light-hail and moderate-rain-shower events at Guiyang Airport on 11 April 2025. The principal conclusions are as follows.

(1) ERA5 fields qualitatively indicated that eastward movement of the mid-tropospheric trough and southward advance of the frontal zone formed the common synoptic background. The juxtaposition of dry, cold lower-tropospheric air and warm, moist flow, together with the evolving shear line and LLJ, was consistent with increased moisture supply, low-level confluence, and an environment favorable for ascent and convective initiation. This interpretation is qualitative because moisture-flux convergence and vertical motion were not diagnosed quantitatively.

(2) Before the light hail, the positive-buoyancy layer was deep, the EL was well above the −20 °C level, and a near-saturated layer spanned the 0 to −20 °C hail-growth zone. Before the moderate rain shower, CAPE was substantially lower, the EL was below the −20 °C level, and positive buoyancy was shallower and less persistent. The principal thermodynamic differences were the depth of convection and the configuration of positive buoyancy relative to the hail-growth zone.

(3) The light-hail stage had comparatively strong deep-layer vertical shear and SRH, accompanied by descending jet-core and strong-wind-layer heights. During the moderate rain shower, wind perturbations were concentrated at lower levels, while deep-layer shear and environmental vorticity support were weaker. LLJI peaks reflected both wind-speed changes and the reduced denominator height. They must be interpreted together with the original wind speed, height, and full wind profile.

(4) The light-hail cell had a stronger and more vertically extensive intense echo core. Its ZDR dipole, local low CC, KDP variability, and the surface hail report jointly supported mixed rain and hail. The moderate-rain-shower cell had a lower intense echo core, positive ZDR, high CC, and more uniform positive KDP. These features were

more consistent with precipitation dominated by liquid raindrops. Radar-derived VIL exceeded 60 kg m^{-2} in the light-hail cell but remained below 20 kg m^{-2} in the moderate-rain-shower cell, further distinguishing the two cells.

These conclusions are based on two convective cells that affected the airport successively during one event. Their generality requires evaluation using additional cases and numerical experiments.

Author Contributions: Conceptualization, G.H., Y.L. and J.Z.; methodology, G.H., L.D., Y.L. and J.Z.; validation, L.D., K.L. and Q.W.; formal analysis, G.H.; investigation, G.H.; resources, F.T. and H.W.; data curation, G.H.; writing—original draft preparation, G.H.; writing—review and editing, G.H., L.D., Y.L., F.T., K.L., J.Z., H.W. and Q.W.; visualization, G.H.; supervision, Y.L. and J.Z.; project administration, Y.L. All authors have read and agreed to the published version of the manuscript.

Funding: This study was supported by the Fundamental Research Funds for the Central Universities (Grant No. 25CAFUC09015) and the Capacity Building for Weather Modification in Southwest China Research and Experiment Project on Detection of Stratocumulus–Cumulus Mixed Clouds and Convective Clouds in Complex Terrain and Artificial Catalysis Technology (Grant No. SCIT-ZG(Z)-2024100001).

Institutional Review Board Statement: Not applicable.

Informed Consent Statement: Not applicable.

Data Availability Statement: The ERA5 reanalysis data used in this study are publicly available from the Copernicus Climate Data Store at https://cds.climate.copernicus.eu/ (accessed on 13 July 2026). The airport observational data supporting the findings of this study are available from the corresponding author upon reasonable request, subject to permission from the relevant data providers. The terrain data in Figure 1a are from the Mapzen Terrain Tiles dataset (https://registry.opendata.aws/terrain-tiles/; accessed on 24 July 2026), combining SRTM, GMTED2010, and ETOPO1.

Conflicts of Interest: Hao Wan is employed by Beijing Airda Electronic Equipment Co., Ltd. Qianpeng Wu is employed by Sichuan Xiwu Laser Technology Co., Ltd. The remaining authors declare no conflicts of interest.

References

1. Hayduk, R.J. Hail damage to typical aircraft surfaces. *J. Aircr.* **1973**, *10*, 52–55. [CrossRef]
2. Proud, S.R. Analysis of aircraft flights near convective weather over Europe. *Weather* **2015**, *70*, 292–296. [CrossRef]
3. Wang, K.Y. Severe turbulence from deep convective clouds during flight SQ321 on 21 May 2024. *Sci. Rep.* **2025**, *15*, 29923. [CrossRef]
4. Illingworth, A.J.; Goddard, J.W.F.; Cherry, S.M. Detection of hail by dual-polarization radar. *Nature* **1986**, *320*, 431–433. [CrossRef]
5. Tang, Z.; Chang, X.; Ni, X.; Xiao, W.; Liu, H.; Guo, J. Evaluation method of severe convective precipitation based on dual-polarization radar data. *Water* **2024**, *16*, 1136. [CrossRef]
6. Straka, J.M.; Zrnić, D.S.; Ryzhkov, A.V. Bulk hydrometeor classification and quantification using polarimetric radar data: Synthesis of relations. *J. Appl. Meteorol.* **2000**, *39*, 1341–1372. [CrossRef]
7. Park, H.S.; Ryzhkov, A.V.; Zrnić, D.S.; Kim, K.E. The hydrometeor classification algorithm for the polarimetric WSR-88D: Description and application to an MCS. *Weather Forecast.* **2009**, *24*, 730–748. [CrossRef]
8. Notaroš, B.M. Polarimetric weather radar: Overview of principles and applications. *IEEE Antennas Propag. Mag.* **2022**, *64*, 43–54. [CrossRef]
9. Askne, J.; Westwater, E.R. A review of ground-based remote sensing of temperature and moisture by passive microwave radiometers. *IEEE Trans. Geosci. Remote Sens.* **1986**, *GE-24*, 340–352. [CrossRef]
10. Solheim, F.; Godwin, J.R.; Westwater, E.R.; Han, Y.; Keihm, S.J.; Marsh, K.; Ware, R. Radiometric profiling of temperature, water vapor and cloud liquid water using various inversion methods. *Radio Sci.* **1998**, *33*, 393–404. [CrossRef]
11. Ware, R.; Carpenter, R.; Güldner, J.; Liljegren, J.; Nehrkorn, T.; Solheim, F.; Vandenberghe, F. A multichannel radiometric profiler of temperature, humidity, and cloud liquid. *Radio Sci.* **2003**, *38*, 8079. [CrossRef]
12. Güldner, J.; Spänkuch, D. Remote sensing of the thermodynamic state of the atmospheric boundary layer by ground-based microwave radiometry. *J. Atmos. Ocean. Technol.* **2001**, *18*, 925–933. [CrossRef]

13. Knupp, K.R.; Coleman, T.; Phillips, D.; Ware, R.; Cimini, D.; Vandenberghe, F.; Vivekanandan, J.; Westwater, E.R. Ground-based passive microwave profiling during dynamic weather conditions. *J. Atmos. Ocean. Technol.* **2009**, *26*, 1057–1073. [CrossRef]
14. Chan, P.W. Performance and application of a multi-wavelength, ground-based microwave radiometer in intense convective weather. *Meteorol. Z.* **2009**, *18*, 253–265. [CrossRef]
15. Cimini, D.; Campos, E.; Ware, R.; Albers, S.; Giuliani, G.; Oreamuno, J.; Joe, P.; Koch, S.E.; Cober, S.; Westwater, E.R. Thermodynamic atmospheric profiling during the 2010 Winter Olympics using ground-based microwave radiometry. *IEEE Trans. Geosci. Remote Sens.* **2011**, *49*, 4959–4969. [CrossRef]
16. Madhulatha, A.; Rajeevan, M.; Venkat Ratnam, M.; Bhate, J.; Naidu, C.V. Nowcasting severe convective activity over southeast India using ground-based microwave radiometer observations. *J. Geophys. Res. Atmos.* **2013**, *118*, 1–13. [CrossRef]
17. Kalapureddy, M.C.R.; Rao, D.N.; Jain, A.R.; Ohno, Y. Wind profiler observations of a monsoon low-level jet over a tropical Indian station. *Ann. Geophys.* **2007**, *25*, 2125–2137. [CrossRef]
18. Bonner, W.D. Climatology of the low-level jet. *Mon. Weather Rev.* **1968**, *96*, 833–850. [CrossRef]
19. Stensrud, D.J. Importance of low-level jets to climate: A review. *J. Clim.* **1996**, *9*, 1698–1711. [CrossRef]
20. Whiteman, C.D.; Bian, X.; Zhong, S. Low-level jet climatology from enhanced rawinsonde observations at a site in the Southern Great Plains. *J. Appl. Meteorol.* **1997**, *36*, 1363–1376. [CrossRef]
21. Weisman, M.L.; Klemp, J.B. The dependence of numerically simulated convective storms on vertical wind shear and buoyancy. *Mon. Weather Rev.* **1982**, *110*, 504–520. [CrossRef]
22. Droegemeier, K.K.; Lazarus, S.M.; Davies-Jones, R. The influence of helicity on numerically simulated convective storms. *Mon. Weather Rev.* **1993**, *121*, 2005–2029. [CrossRef]
23. Rasmussen, E.N.; Blanchard, D.O. A baseline climatology of sounding-derived supercell and tornado forecast parameters. *Weather Forecast.* **1998**, *13*, 1148–1164. [CrossRef]
24. Thompson, R.L.; Mead, C.M.; Edwards, R. Effective storm-relative helicity and bulk shear in supercell thunderstorm environments. *Weather Forecast.* **2007**, *22*, 102–115. [CrossRef]
25. Testud, J.; Le Bouar, E.; Obligis, E.; Ali-Mehenni, M. The rain profiling algorithm applied to polarimetric weather radar. *J. Atmos. Ocean. Technol.* **2000**, *17*, 332–356. [CrossRef]
26. Gorgucci, E.; Scarchilli, G.; Chandrasekar, V.; Meischner, P.F.; Hagen, M. Intercomparison of techniques to correct for attenuation of C-band weather radar signals. *J. Appl. Meteorol.* **1998**, *37*, 845–853. [CrossRef]
27. Böck, T.; Löffler, M.; Marke, T.; Pospichal, B.; Knist, C.; Löhnert, U. Instrument uncertainties of network-suitable ground-based microwave radiometers: Overview, quantification, and mitigation strategies. *Atmos. Meas. Tech.* **2025**, *18*, 6251–6270. [CrossRef]
28. Shrestha, B.; Brotzge, J.A.; Wang, J. Evaluation of the New York State Mesonet Profiler Network data. *Atmos. Meas. Tech.* **2022**, *15*, 6011–6033. [CrossRef]
29. Qi, Y.; Guo, Y. A quality control method and implementation process of wind profiler radar data. *Atmosphere* **2022**, *13*, 796. [CrossRef]
30. Wilson, J.W.; Roberts, R.D. Summary of convective storm initiation and evolution during IHOP: Observational and modeling perspective. *Mon. Weather Rev.* **2006**, *134*, 23–47. [CrossRef]
31. Mueller, C.K.; Saxen, T.; Roberts, R.; Wilson, J.; Betancourt, T.; Dettling, S.; Oien, N.; Yee, J. NCAR Auto-Nowcast System. *Weather Forecast.* **2003**, *18*, 545–561. [CrossRef]
32. Dixon, M.; Wiener, G. TITAN: Thunderstorm identification, tracking, analysis, and nowcasting: A radar-based methodology. *J. Atmos. Ocean. Technol.* **1993**, *10*, 785–797. [CrossRef]
33. Cintineo, J.L.; Pavolonis, M.J.; Sieglaff, J.M. ProbSevere Version 3: Improved exploitation of data fusion and machine learning for nowcasting severe weather. *Weather Forecast.* **2024**, *39*, 1937–1958. [CrossRef]
34. Wang, Q.; Zhang, Y.; Liu, L. Impact of optical flow and joint loss on nowcasting of severe convective weather at airports. *Atmosphere* **2026**, *17*, 497. [CrossRef]
35. Kahraman, A.; Kendon, E.J.; Fowler, H.J.; Short, C.J. Future changes in severe hail across Europe, including regional emergence of warm-type thunderstorms. *Nat. Commun.* **2025**, *16*, 8438. [CrossRef]
36. Liu, S.; Zheng, Y.; Tao, Z. The analysis of the relationship between pulse of low-level jet and heavy rain using wind-profiler data. *J. Trop. Meteorol.* **2003**, *19*, 285–290. (In Chinese) [CrossRef]
37. Huang, X.; Sun, J.; Liu, W. The interaction between low-level jet evolution and severe convective rainstorms under topographic effect. *Acta Meteorol. Sin.* **2020**, *78*, 551–567. (In Chinese) [CrossRef]
38. Shi, Y.R.; Shou, S.W.; Wang, L.R.; Yang, R.Z.; Zhao, Y.C. Relationship between storm relative helicity and types of strong convective weather. *J. Meteorol. Environ.* **2011**, *27*, 65–71. (In Chinese)
39. Ni, C.; Li, G.; Zhang, J.; Niu, J.; Chen, H. Wind field analysis of a hailstorm event in Chengdu mountainous area in spring based on wind profile radar. *Desert Oasis Meteorol.* **2025**, *19*, 130–136. (In Chinese) [CrossRef]
40. Engerer, N.A.; Stensrud, D.J.; Coniglio, M.C. Surface characteristics of observed cold pools. *Mon. Weather Rev.* **2008**, *136*, 4839–4849. [CrossRef]

41. Guo, X.; Huang, M. Hail formation and growth in a 3D cloud model with hail-bin microphysics. *Atmos. Res.* **2002**, *63*, 59–99. [CrossRef]
42. Smith, T.M.; Lakshmanan, V.; Stumpf, G.J.; Ortega, K.L.; Hondl, K.; Cooper, K.; Calhoun, K.M.; Kingfield, D.M.; Manross, K.L.; Toomey, R.; et al. Multi-Radar Multi-Sensor (MRMS) Severe Weather and Aviation Products: Initial Operating Capabilities. *Bull. Am. Meteorol. Soc.* **2016**, *97*, 1617–1630. [CrossRef]
43. Allen, J.T.; Giammanco, I.M.; Kumjian, M.R.; Punge, H.J.; Zhang, Q.; Groenemeijer, P.; Kunz, M.; Ortega, K. Understanding hail in the Earth system. *Rev. Geophys.* **2020**, *58*, e2019RG000665. [CrossRef]
44. Yi, N.; Su, L.; Zheng, X.; Xin, Y.; Cai, M.; Li, H.; Jin, Y. Environmental parameters and forecast models of hail events. *Arid Zone Res.* **2024**, *41*, 13–23. (In Chinese) [CrossRef]

Disclaimer/Publisher's Note: The statements, opinions and data contained in all publications are solely those of the individual author(s) and contributor(s) and not of MDPI and/or the editor(s). MDPI and/or the editor(s) disclaim responsibility for any injury to people or property resulting from any ideas, methods, instructions or products referred to in the content.